Advances in Science and Technology Research Journal

Advances in Science and Technology Research Journal, 2026, 20(3), 129–147
https://doi.org/10.12913/22998624/213903
ISSN 2299-8624, License CC-BY 4.0

Received: 2025.10.23
Accepted: 2025.12.03
Published: 2026.02.01

Influence of oxalic acid and seawater in iron-based binders: Correlating porosity with compressive strength through image processing

Viswanathan Chandralega[1], Muthusamy Shanmugasundaram[1*]

[1] School of Civil Engineering, Vellore Institute of Technology, Chennai, 600127, India
* Corresponding author's e-mail: shanmuga.sundaram@vit.ac.in

ABSTRACT

This study investigated the feasibility of iron-based binders under CO_2 curing and the development of sustainable construction materials. Samples were prepared using varying concentrations of oxalic acid (0%, 2%, and 4%) using different mixing media (normal water and seawater), and their mechanical properties (compressive and flexural strength) and microstructural characteristics were evaluated. The results demonstrate that the best-performing oxalic acid concentrations – 2% for normal water and 4% for seawater, which enhances compressive and flexural strengths by promoting carbonation reactions, leading to denser microstructures and the formation of stable carbonate phases. Excessive oxalic acid, however, hampers phase development and reduces strength due to increased acidity, porosity, and formation of weaker phases. Microstructural analysis revealed that moderate additions facilitate uniform pore distribution and controlled porosity, which accelerates carbonation and densification, while higher dosages or larger interconnected pores diminish performance. The mineral content of seawater, including Mg^{2+}, Cl^-, and SO_4^{2-}, synergistically interacts with oxalic acid to further enhance carbonation, resulting in superior mechanical strength and structural integrity compared to normal water. These findings emphasize the importance of optimizing additive contents and leveraging seawater chemistry to develop sustainable, high-performance iron-based binders with improved microstructural and mechanical properties.

Keywords: iron-binder, seawater, image processing, compressive strength, porosity, carbon capture.

INTRODUCTION

Global industrialization has driven significant advancements in infrastructure, technology, and economic growth, bringing sustainability challenges to greenhouse gas emissions. The reliance on fossil fuels for transportation, energy production, and industrial applications has led to the release of greenhouse gases into the atmosphere [1]. These intensified greenhouse gas accumulations have led to increases in global temperature, sea level, and frequent extreme weather conditions. In 2019, the average atmospheric concentration of carbon dioxide (CO_2) was reported as 414.7 ppm, which is a 45% increase from 1980–1990 [2]. Over the past decades, CO_2 emission levels have increased by more than 2 ppm annually, with a 400% increase since 1950 due to human-induced activities [3]. CO_2 emissions reduction can be achieved by adopting various renewable energy sources, including solar, wind, tidal, and hydrogen energy, to replace fossil fuel energy [4]. However, these techniques are long-term processes, which in turn lead to the adoption of trends in carbon capture, utilization, and storage (CCUS) techniques for CO_2 reduction. CCUS refers to the overall CO_2 capture process from sources such as industrial plants, and reusing or storing it to prevent substantial release into the atmosphere. Carbon capture and Storage (CCS) is widely used in many industrial applications, including power generation, and can sequester approximately 7 billion tons of CO_2 annually by 2050 [5]. CCS involves storing CO_2 in the deep

ocean reservoirs or deep geological formations, while Carbon Capture and Utilization (CCU) convert CO_2 into a stable product by reacting it with industrial by-products or feedstock. CCU technology can be applied to industrial by-products to transform waste into construction materials, thereby contributing to a carbon-neutral circular economy [6]. According to the International Energy Agency (IEA), widespread deployment of CCS is expected to reduce greenhouse gas (GHG) emissions by approximately 55% [7]. Mineral carbonation is considered a low-risk and long-term sustainable process for CO_2 sequestration, which helps mitigate up to 3 Gt of carbon emissions per year by 2030 [8]. Mineral carbonation is an engineered and natural process that involves the reaction of earth metals, such as calcium (Ca) and magnesium (Mg) ions, with CO_2 to form stable carbonate minerals. Industrial solid wastes, including coal-fired products, iron or steel slag, red mud, cement/concrete wastes, mining wastes, and mineral processing wastes, are widely adopted for CO_2 mineralization technology [9–12]. There are concerns regarding the stabilization and re-utilization of alkaline solid waste because it contains highly unstable calcium oxide and magnesium oxides [13]. In recent years, many researchers have focused on the reaction of metal oxides with CO_2 to produce metal carbonates. Compared to silicate, calcium, and magnesium minerals, alkaline solid waste has a smaller particle size, higher reactivity, and does not require any pretreatments to react with CO_2 to form carbonates [14, 15].

Iron oxide magnetite (Fe_3O_4) is a key ingredient and a low-cost material used in the manufacture of iron (Fe) [16–18]. According to acid-base interactions, metal oxides such as Al_2O_3, TiO_2, and Fe_3O_4 have active sites on their surfaces that can react with gaseous molecules, including CO_2, O_2, NH_3, CO, and H_2O. Fe_3O_4 has significant potential for adsorbing CO_2 and interacting with H_2O, influencing carbonation reactions and resulting in stable carbonate products [19, 20]. Recent research has demonstrated the use of Fe_3O_4 and Fe as active materials under carbon curing. Iron is an efficient reducing agent because of its thermodynamic properties, which are involved in chemical reactions during carbon capture and utilization. The study examined the transportation and adsorption of CO_2 molecules within the nanoporous structures of iron oxides like FeO and Fe_2O_3, offering insights into optimized utilization of iron-rich industrial residues in carbon curing [21]. The viability of using iron mining waste in mineral carbonation for CO_2 sequestration was studied, suggesting that the alkaline nature and presence of Fe, Ca, and Mg-bearing minerals are essential for forming stable carbonates [22]. The study also showed that increasing pH to 12 and reducing particle size below 38 μm improved carbonation efficiency for Fe and Ca. During the carbon capture process, iron oxides are synthesized into siderite ($FeCO_3$), which involves the chemical reaction of iron oxides and ferrous oxalate with CO_2 to produce iron (II) carbonate as shown in Equation 1 and Equation 2. [16].

$$Fe_3O_4(s) + Fe(s) + 4CO_2(g) \rightarrow 4FeCO_3(s) \quad (1)$$

$$Fe_2O_3(s) + Fe(s) + 3CO_2(g) \rightarrow 3FeCO_3(s) \quad (2)$$

Both natural alkaline minerals and industrial waste can be employed to achieve CO_2 mineralization. The effectiveness of CO_2 mineralization of natural alkaline minerals is limited compared to that of industrial waste. Natural mineral-based CO_2 mineralization has slow reaction kinetics that can be improved by involving high-energy solutions such as mechanical grinding and chemical, mechanical, and thermal pretreatment [23]. Among these, fly ash (FA) obtained from coal combustion power plants has high alkalinity and is a promising material for CO_2 sequestration. Studies have revealed that FA, with a suitable chemical composition, particle size, temperature, pressure, and CO_2 concentration, can effectively sequester CO_2 [24]. The utilization of FA reduces the moisture content in the matrix and improves the pore connectivity, creating pathways for CO_2 for increased CO_2 absorption [25]. The effect of CO_2 mineralization on fly ash was studied on variations in water-to-solid ratio and CO_2 pressures, where the variation in pressure impacts CO_2 capture, reacting with portlandite to form calcite ($CaCO_3$) [26]. Silica-rich fly ash, along with metakaolin, provides cohesive binding properties, and limestone powder acts as a nucleating agent that was adopted for the experiments [27, 28]. The combination of iron powder, fly ash, metakaolin, and calcium carbonate, along with varying oxalic acid, yields an iron binder matrix [29]. Seawater was used as the solvent for mixing the binder in this research to investigate the performance of the iron-binder matrix [29]. Seawater exhibits promising potential for CO_2 mineral carbonation owing to its

high salinity and naturally high concentrations of calcium (Ca^{2+}) and magnesium ions (Mg^{2+}) [30]. The number of divalent cations present in seawater actively contributes to the carbonation reaction and promotes a high carbonation efficiency [31]. The efficiency of the mineralization of CO_2 using seawater is studied, as it offers several advantages, including widespread availability, low acquisition cost, minimum environmental impact, highlighting the efficiency of carbonation, and developing sustainable CCU strategies [32]. This addition introduced chloride ions into the binder and explored the chloride binding capacity and carbonation mechanisms of the iron binder [33]. Oxalic acid ($C_2H_2O_4$) is a strong acidic dicarboxylate that acts as both a reducing and chelating agent for iron compounds, which is widely used to dissolve iron oxides and modify binder chemistry [34]. Previous studies have shown that oxalate-related dissolution of iron oxide influences leaching, which is strongly dependent on factors such as pH, temperature, and mineral phases [35]. In cementitious and alternative binder systems, chelators like oxalic acid promote ion mobility and increase the precipitation of carbonate phases during the CO_2 curing mechanisms, resulting in dense pore structure and enhanced strength gain even at lower dosages. Conversely, in glass ionomer systems, oxalic acid can act as a reaction modifier, where it influences the working and setting time by considering the surface hardening due to the precipitation of metal oxalates, which influences the microstructural characteristics. These findings suggest that oxalic acid has the potential to accelerate carbonation reactions and influence the microstructure of iron-based binders, depending on the dosage level, pH, temperature, and CO_2 curing conditions [36].

The goal of this study is to investigate the mechanical performance of seawater in an iron binder with varying amounts of oxalic acid (0%, 2%, and 4%), as well as the performance of the samples using media such as normal water and seawater with oxalic acid proportions. The investigation examines compressive strength, flexural strength, and microstructural characteristics of the iron binders with varying concentrations of oxalic acid in different media. In this study, the pore radius and porosity were determined using image processing techniques, which offer a novel area for iron-based binders in CO_2 curing conditions.

MATERIALS AND TESTING METHODS

Raw materials

The following raw materials were used to prepare the iron carbonate-based binder specimens: iron powder, fly ash, metakaolin, and calcium carbonate. Iron powder was sourced from Civitech Engineering Pvt. Ltd, which mainly consists of Fe_2O_3, SiO_2, and Al_2O_3. Class F fly ash, metakaolin, calcium carbonate, and oxalic acid were acquired from Astra Chemicals, Chennai. Fly ash contains oxides such as SiO_2, Al_2O_3, and CaO. Metakaloin contains oxides such as SiO_2, Al_2O_3, and TiO_2. And calcium carbonate consists mainly of oxides of SiO_2, Al_2O_3, and CaO. The particle sizes and chemical compositions of the raw materials were characterized to determine their physical properties. A Laser Diffraction Particle Size Analyzer (CILAS-1180) was used to analyze the particle size distribution of the raw materials, as shown in Figure 1. Table 1 shows the chemical composition of the raw materials obtained by X-ray fluorescence spectrometry (XRF) at CSIF, University of Calicut. Additionally, Figures 1(a) and (b) also demonstrate the crystalline phases of the raw materials used, which were determined through X-ray diffraction analysis (XRD) and micromorphology through scanning electron microscopy (SEM) images.

Figure 1 shows the SEM-EDS and XRD results of the raw ingredients used in the iron binder matrix. Iron powder (IP) exhibited angular particles with rough surface textures in SEM, and EDS analysis revealed peaks of Fe and O, confirming the presence of iron oxides. The XRD observations show major peaks of magnetite and iron and a minor peak of quartz. Magnetite (Fe_3O_4) and metallic iron (Fe) are highly crystalline, which is essential for higher reactivity. For fly ash (FA), the SEM image confirms the typical morphology of spherical particles, while the EDS spectra show a significant presence of Si, Al, O, Mg, Ca, and Fe. In the XRD analysis, a rich source of silica and alumina (mullite) was present, which promoted iron silicate formation upon reaction. The metakaolin SEM image revealed a heterogeneous microstructure with fine particles of Si, Al, O, and some traces of Ti and Fe, as shown by EDS. The XRD pattern shows the presence of both crystalline peaks (quartz and hematite) and amorphous peaks (dehydroxylated kaolinite), which indicates that it has a carbon

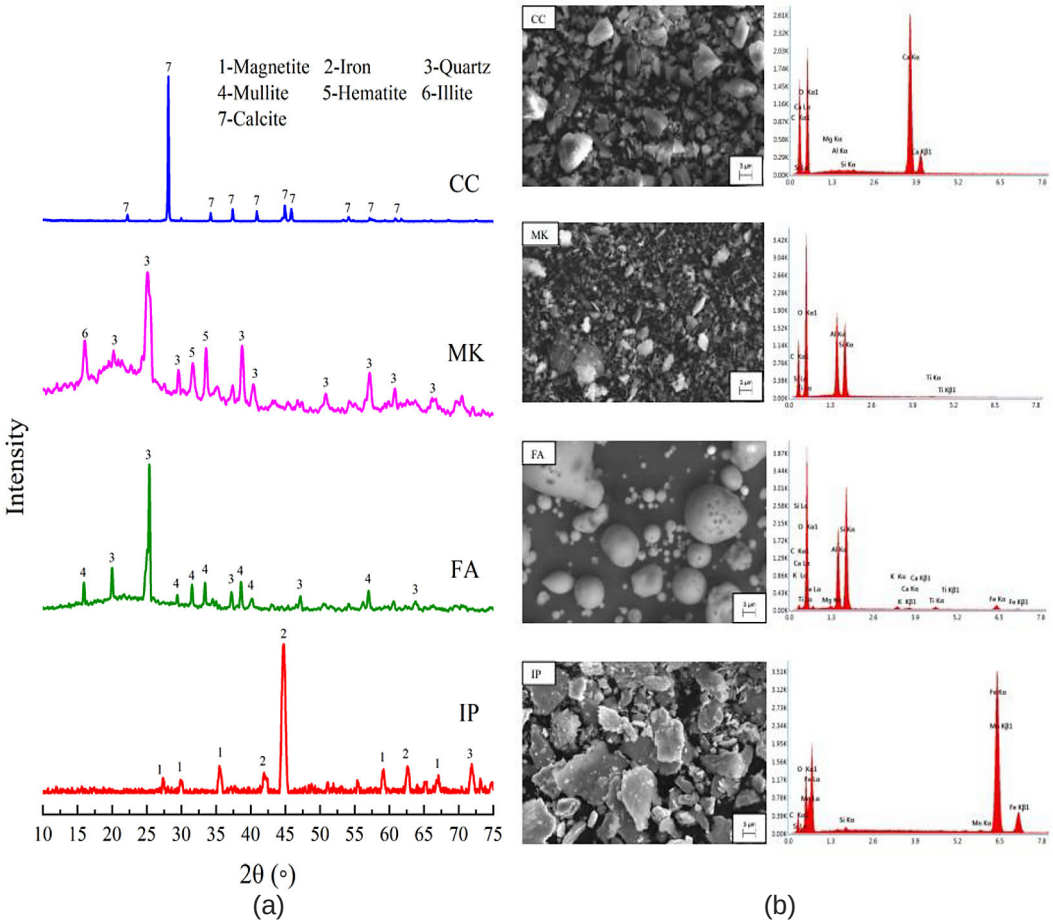

Figure 1. (a) XRD, (b) micromorphology and elemental distribution of raw materials: iron powder (IP), Fly ash (FA), metakaolin (MK), calcium carbonate (CC)

Table 1. Compositional analysis of the raw materials using XRF

Composition (wt%)	Iron powder	Fly ash	Metakaolin	Calcium carbonate
Fe_2O_3	87.32	2.95	0.54	-
SiO_2	1.323	57.38	50.2	0.142
Al_2O_3	0.3365	36.11	46.7	0.087
CaO	-	0.7882	0.09	99.45
P_2O_5	0.3486	0.374	0.39	0.002
MgO	0.159	1.007	0.17	-
SO_3	0.1858	0.0397	0.03	-
Na_2O	-	-	-	-
TiO_2	0.0024	0.8237	1.47	-
K_2O	0.0055	0.7468	0.12	0.006

capture efficiency when blended. The SEM image of calcium carbonate confirmed the presence of irregular particles with a dense microstructure. EDS observation revealed strong peaks of Ca, C, and O, indicating the formation of crystalline calcite ($CaCO_3$). The higher crystalline nature of calcite improves the packing density and provides nucleation sites for hydration.

The raw materials were well-graded particles, as shown in Table 2, with particle sizes ranging (d10 to d90) from 10.35 µm to 88.87 µm for iron powder, 4.48 µm to 146.10 µm for fly ash, 1.61 µm to 18.80 µm for metakaolin, and 2.03 µm to 17.02 µm for calcium carbonate. Particle size analysis revealed that calcium carbonate and metakaolin had smaller particle sizes,

whereas iron powder and fly ash had coarse particles. In addition, along with the above-mentioned raw materials, oxalic acid is used as a chelating agent for leaching iron to form iron oxalate [35].

Preparation of the test samples and carbonation regimes

Six iron-based binder samples, denoted as NW-0, NW-2, NW-4, SW-0, SW-2, and SW-4, were prepared using variations in oxalic acid at 0%, 2%, and 4% with normal water and seawater, with the other raw ingredients, as shown in Figure 2. Table 4 indicates the mix proportion of raw materials for the iron binder mix with normal water and seawater, along with oxalic acid variations. Water-to-binder (w/b) ratio was adopted as 0.27 with the variation of oxalic acid along with normal water (potable water) from the laboratory, and seawater was collected from Kovalam Beach, Chennai. The chemical composition of the collected seawater is represented in Table 3.

The samples were prepared using a mechanical stirrer by primarily adding the raw materials with oxalic acid and the required amount of water at a low speed for 2 min, and thoroughly mixing at a high speed of 125 RPM (revolutions per minute) for 3 min at room temperature. The freshly prepared iron binder mixture was placed on steel cubes and prism molds, vibrated, and the surface was finished with a trowel. The samples were immediately transferred into the carbonation chamber and it is filled with carbon dioxide gas, and cured for five days, as shown in Figure 3. The chamber was maintained at 30 ± 2 °C and 85 ± 5% relative humidity (RH).

In this study, oxalic acid is added in varying concentrations at 0%, 2% and 4% to analyze its influence on the iron binder in carbonation reactions under CO_2 curing. A control sample is adopted to study the baseline performance of the iron-based binder in the absence of the chelating agent under CO_2 curing. While the 2% addition is selected based on the preliminary trials and supporting previous literature, which promotes the

Table 2. Physical properties of raw materials

Property	Iron powder	Fly ash	Metakaolin	Calcium carbonate
d_{10} (µm)	10.35	4.48	1.61	2.03
d_{50} (µm)	36.23	43.78	6.23	9.24
d_{90} (µm)	88.87	146.10	18.80	17.02
Mean diameter (µm)	43.68	61.48	8.43	9.47

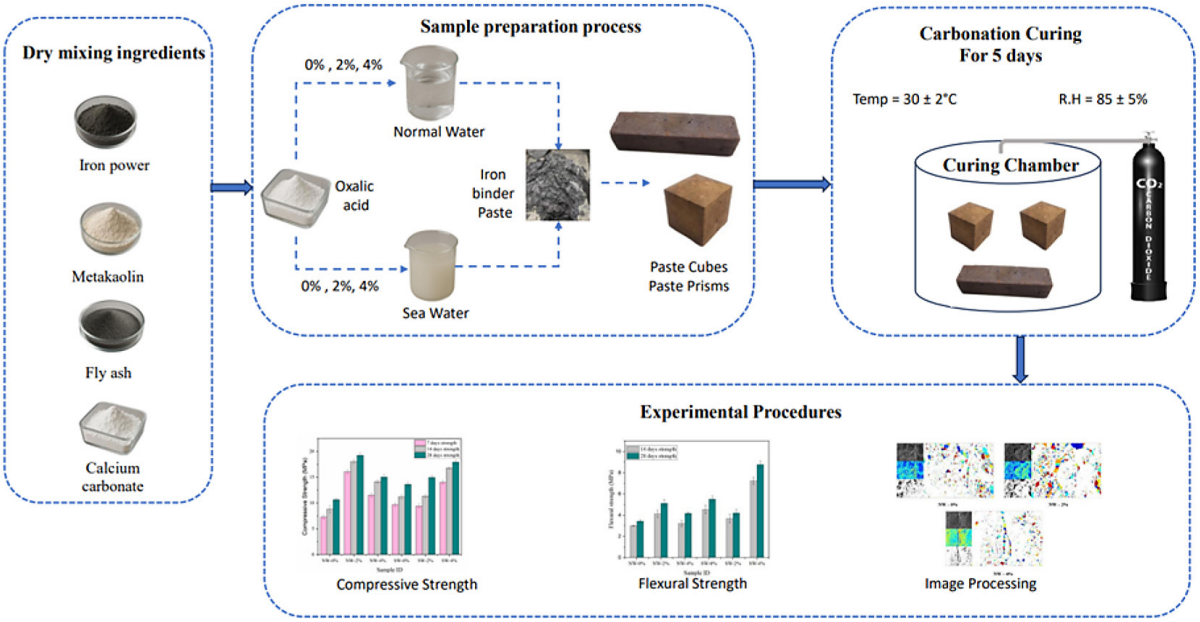

Figure 2. Graphical representation of the experimental procedure

Table 3. Chemical compositions of seawater

Component	Mg^{2+} (ppm)	Na^{+} (ppm)	SO_4^{2-} (ppm)	Cl^{-} (ppm)	Inorganic solids (ppm)	Organic solids (ppm)	Electrical conductivity (µmhos/cm)
Concentration	1433	10,897	2628	19,743	27,946	37,715	43,285

Table 4. Mix proportions of iron-based binder (percentage by mass of total powder per kilogram)

Sample ID*	Iron powder (grams)	Fly ash (grams)	Calcium carbonate (grams)	Metakaolin (grams)	w/b ratio (l/kg)	Oxalic acid (grams)
NW-0	612.33	204	81.67	102	0.27	0
NW-2	600	200	80	100	0.27	20
NW-4	588	196	78.33	97.67	0.27	40
SW-0	612.33	204	81.67	102	0.27	0
SW-2	600	200	80	100	0.27	20
SW-4	588	196	78.33	97.67	0.27	40

Note: *NW-0, NW-2, NW-4, and SW-0, SW-2, SW-4 represent the normal water and seawater sample mix at 0%, 2%, and 4% variations of oxalic acid, respectively.

iron dissolution and enhances the carbonation reaction. And the 4% addition of oxalic acid is adopted to further study the effect of the chelating agent in higher concentrations and its influence on carbonation reactions. These concentrations of oxalic acid were adopted to understand both the beneficial and limiting effects of the practical percentage range, providing deeper insights into the mechanical and microstructural properties.

EXPERIMENTAL PROCEDURES

Compressive strength test

Under IS:516-2021, the compressive strength was evaluated using a 50 mm cube specimen prepared with an iron binder. The compressive strength test was conducted at 7, 14, and 28 days using a CTM with a maximum 2000 kN capacity (Shimadzu, Concreto 2000X). The compressive strength was obtained from the average values of the three tested samples. Specifically, the cube samples were tested under compression at a loading rate of 0.5 MPa/s, and constant loading was applied until the specimens were fractured completely.

Flexural strength test

The flexural strength was evaluated by testing 40 × 40 × 160 mm prism samples at 14 and 28 days as per IS:516-2021. Universal Testing Machine (UTM) from SHIMADZU with 50 kN capacity is applied at a loading rate of 0.06 $N/mm^2/s$ by the three-point loading method to determine the flexural strength.

Image processing

An image processing algorithm was employed to determine the pore sizes from the scanning electron microscope (SEM) images. These algorithms consist of five steps, as represented in Figure 4: (1) image acquisition, (2) pre-processing, (3) segmentation, (4) morphological operations, (5) porosity analysis, and (6) data visualization [37]. Each SEM image was passed through Otsu's multi-level thresholding, which includes 6 levels of quantization that detect the darkest portion in the image. After thresholding, the median filter is applied to reduce noise, and then a city-block distance is used to transform it into a binary image to highlight pore centres. These algorithms effectively differentiate the overlapping of closed porous structures, facilitating the calculation of the average pore size and distribution. The segmentation process involves city-block distance transforms to measure the pixel intensity distances, which aids in the separation of adjacent pores. A median filter was employed before segmentation to minimize noise and enhance the image quality. This filtering helps to remove small artifacts while preserving the critical pore boundaries effectively. Finally, segmented pore regions are analyzed to evaluate the average pore size, and the results are visualized to provide a clear understanding of porous structures and their characteristics [38].

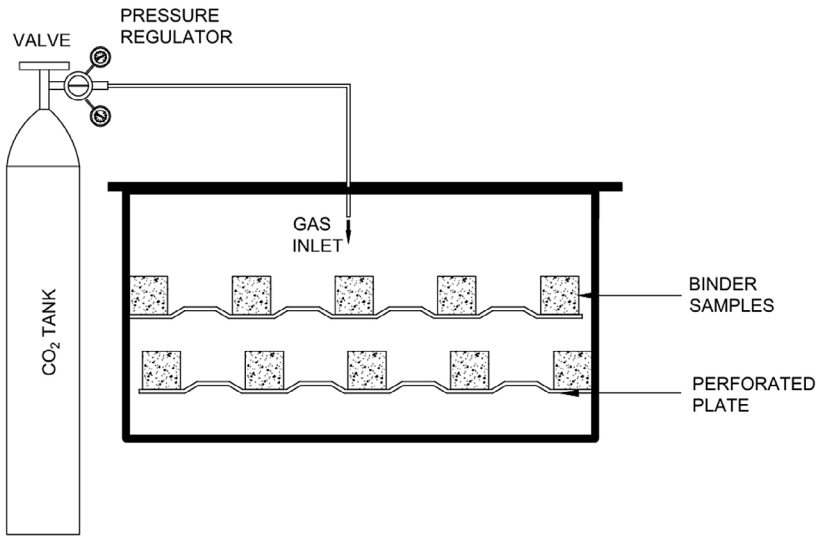

Figure 3. Schematic diagram of the CO_2 curing chamber set-up

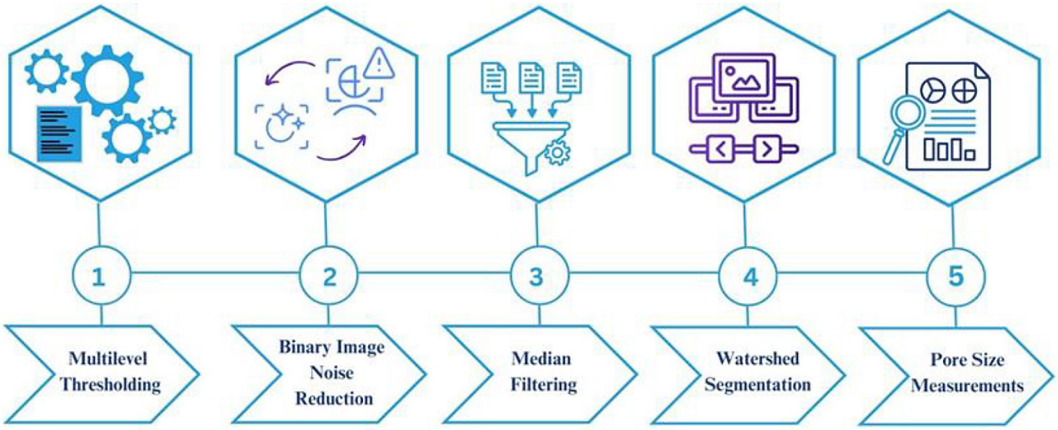

Figure 4. Image processing workflow for porosity measurement of iron-based binder

RESULTS AND DISCUSSION

Dry unit weight

The dry unit weight of the iron-based binder provides a relationship between physical properties and mechanical strength, reflecting the degree of densification and carbonate formation during CO_2 curing. The Figure illustrates the variation in dry unit weight with compressive strength at 7, 14, and 28 days. The variation in dry unit weight in iron binder samples demonstrates the densification of the matrix and the development of strength reactions. NW-0 showed an increase in dry unit weight from 7 days (2000 kg/m^3) to 14 days (2200 kg/m^3), followed by a slight decrease to 2077 kg/m^3 at 28 days. This indicates that the absence of oxalic acid limited the densification of the matrix. The NW-2 sample exhibited a higher dry unit weight at 7 days (2080 kg/m^3) and 14 days (2320 kg/m^3), and stabilized at 28 days (2154 kg/m^3), indicating that oxalic addition promotes dissolution and carbonate precipitation. The moderate addition of oxalic acid enhances the transportation of Fe through dissolution, which accelerates the formation of siderite/calcite ($FeCO_3$/$CaCO_3$) [35]. Conversely, NW-4 achieved comparatively lower density values, ranging from 2040 kg/m^3 to 2039 kg/m^3, from 7 to 28 days, indicating that the excess addition of oxalic acid hindered the carbonation reaction due to over-chelation of iron ions. In the SW series, the dry unit weight of SW-0 samples reached a peak value of 2720 kg/m^3 at 14 days and decreased to 2231 kg/m^3 at 28 days, indicating a more porous formation of the sample. Similarly, SW-2 exhibited high unit weight at 14 days (2640 kg/m^3) and dropped to 2115 kg/m^3 at 28 days, suggesting that the effects

of both oxalic acid and seawater reduced the formation of densified matrix. In SW-4, the unit weight values increase from 2200 kg/m^3 at 7 days to 2320 kg/m^3 at 14 days and remain at 2231 kg/m^3 at 28 days. This indicates that a stabilized carbonation reaction occurs between the seawater and oxalic acid. The seawater ions help in early carbonate precipitation from CO_2 uptake. Comparing both normal water and seawater samples, compressive strength follows a similar trend with the variations in dry unit weight, confirming that the strength gain is primarily due to the densification of the matrix and carbonate precipitation.

Compressive strength

The compressive strength of the normal water samples showed a clear trend under the influence of oxalic acid in the iron-based binder samples, as shown in Figure 5. The NW-0 sample exhibited the lowest strength at 7, 14, and 28 days, with values of 7.3 MPa, 8.8 MPa, and 10.65 MPa, respectively. Whereas the NW-2 and NW-4 samples exhibited an increase in strength with the addition of oxalic acid. The 2% addition of oxalic acid achieved higher strengths of 16.07 MPa at 7 days, 18.04 MPa at 14 days, and 19.24 MPa at 28 days, indicating about an 80.7% increase in strength over 0% oxalic acid. The NW-4 samples represent 41.1% higher strength than NW-0, attaining strengths of 11.52 MPa at 7 days, 14.16 MPa at 14 days, and 15.03 MPa at 28 days, but remained lower than NW-2.

This indicates that oxalic acid plays a crucial role in enhancing carbonation reactions, leading to a denser microstructure and higher strength, owing to the stronger formation of stable carbonates. The interaction between oxalic acid and iron plays a vital role in influencing the formation of carbonate phases during CO_2 exposure. Oxalic acid acts both as a catalyst and dissolution agent for iron, contributing to the higher strength observed in NW-2. The enhanced dissolution of iron is facilitated by the chelating effect of oxalic acid, which is attributed to the greater availability of Fe^{2+} and Fe^{3+} ions to react with CO_2 to form iron carbonate $FeCO_3$ (siderite) and iron hydr(oxide) phases (Fe_2O_3 and Fe_3O_4), contributing to matrix development [39, 40]. This process enhances the mobility of the iron ions by producing Fe-oxalate complexes (Fe^{2+}/Fe^{3+}), facilitating their availability for carbonation reactions. Under CO_2 curing, the released iron ions react with the carbonate ions to form siderite, which contributes to the strength development[34]. However, the results also indicate that the excessive addition of oxalic acid would be counterproductive, as evidenced in the NW-4 samples. In addition, the lower strength gains in NW-4 demonstrate that excess oxalic acid may hinder the strength gain due to the formation of weak phases and increased porosity in the samples. This phenomenon may be attributed to changes in the reaction kinetics and oversaturation, which can disrupt proper phase formation or acid-induced porosity with carbonate precipitation [41]. It was concluded that the carbonation reaction of normal water with acid-promoted iron dissolution lacks additional reactive cations, such as Ca^{2+} and Fe^{2+}, forming secondary minerals. The excessive addition of oxalic acid may lead to the precipitation of an insoluble form of ferrous oxalates and calcium oxalates by forming immediate crystalline solid particles on the surface, which blocks further reaction of the ions to react with CO_2 to form carbonates[35]. This finding highlights the importance of selecting an oxalic acid content in iron-based binders to strike a balance between enhanced carbonation reactions and favorable microstructural properties [42]. While NW-2 has attained the highest strength in this study, further research may be carried out to determine the oxalic acid concentration for maximum strength gain and durability in iron-binder systems.

The seawater (SW) samples also showed a similar trend, where the addition of oxalic acid significantly improved the compressive strength, as shown in Figure 5.

SW–0 sample recorded lower strengths of 9.67 MPa at 7 days, 11.22 MPa at 14 days, and 13.62 MPa at 28 days, while strength improvement was evident in SW-2 and SW-4 samples. With 2% addition of oxalic acid (SW-2), the strength increased to 9.4 MPa at 7 days, 11.34 MPa at 14 days, and 14.96 MPa at 28 days, indicating about a 9.48% increase in strength over SW-0 samples at 28 days. SW-4 samples show the highest compressive strength, attaining 14.02 MPa at 7 days, 16.78 MPa at 14 days, and 17.93 MPa at 28 days, which is about a 31.65% increase in strength compared to SW-0 at 28 days.

These results suggest that an increase in the addition of oxalic acid aids the formation of stable carbonate phases in the seawater-based iron binder matrix. The improved strength is attributed to the synergistic effect of oxalic acid and ions in seawater, including Mg^{2+}, Ca^{2+}, Cl^-, Na^+,

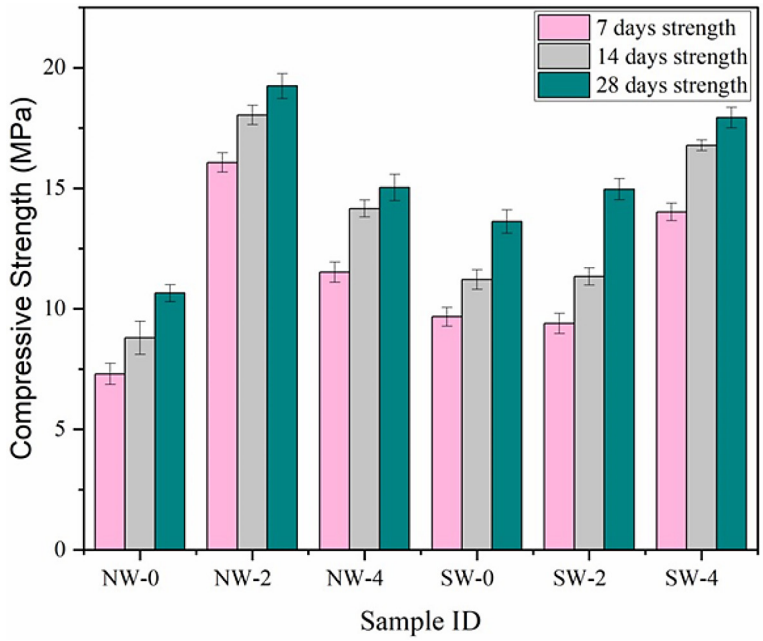

Figure 5. Compressive strength of normal water and seawater samples.

and SO_4^{2-}, which accelerate iron dissolution and facilitate the interaction between iron ions (Fe^{2+}) and CO_2 molecules during carbonation [35]. The reaction mechanisms usually involve three steps: (i) separation of calcium/ iron/ magnesium ions from alkaline materials (FA, Iron powder); (ii) the dissolution of CO_2 gas molecules into the aqueous phase; and (iii) precipitation of carbonates through the reaction of CO_2 gas molecules with Ca^{2+}, Fe^{2+}, and Mg^{2+} ions [43, 44]. The magnesium ions in seawater interact with oxalic acid, contributing to strength development through the formation of hydromagnesite, a supplementary reaction product. Seawater has a naturally higher pH (approximately 8.1 to 8.3) than normal water, which improves the dissolution kinetics of CO_2 and shifts the equilibrium towards carbonate ion formation, enhancing the precipitation of carbonates [45]. This trend in compressive strength highlights the role of oxalic acid interaction with seawater ions in the development of mechanical properties [46, 47]. The increase in oxalic acid concentration promoted the dissolution of iron particles, influencing the reaction kinetics because of the higher ionic strength, solubility, and diffusion of CO_2, leading to the formation of more stable carbonates [48, 34]. The absence of oxalic acid resulted in fewer carbonation reactions and, consequently, lower mechanical strength in the SW-0 samples. Optimizing the oxalic acid content in seawater-based iron binders can be an effective strategy for developing a binder with enhanced mechanical and microstructural integrity. The ionic presence in seawater influenced the carbonation reactions in the iron binder system. Chloride and sulphate ions were available for enhancing the dissolution and precipitation kinetics during CO_2 curing. Chloride ions increase the ionic strength in the pore solution and promote calcium ion dissolution from calcium, thereby facilitating the availability of Ca^{2+} and Fe^{2+} for further precipitation [31]. While sulphate ions interact with Ca^{2+} to form sulphate-bearing phases, this creates favourable conditions for CO_2 uptake. The combined presence of seawater ions such as Mg^{2+}, Ca^{2+}, Cl^-, Na^+, and SO_4^{2-} further enhances nucleation and formation of carbonate phases, leading to increased carbonation efficiency and microstructural refinement [31, 45, 49, 50].

Flexural strength

Figure 6 illustrates the correlation between flexural strength and oxalic acid concentration for normal water (NW) and seawater (SW) samples at 14 and 28 days. For normal water samples, the flexural strength at 14 days increased from approximately 3.0 MPa (NW-0) to 4.1 MPa (NW-2), demonstrating that 2% oxalic acid improves early-age strength. However, there seems to be a slight decrease to 3.2 MPa (NW-4), suggesting that additional oxalic acid may hinder the formation of

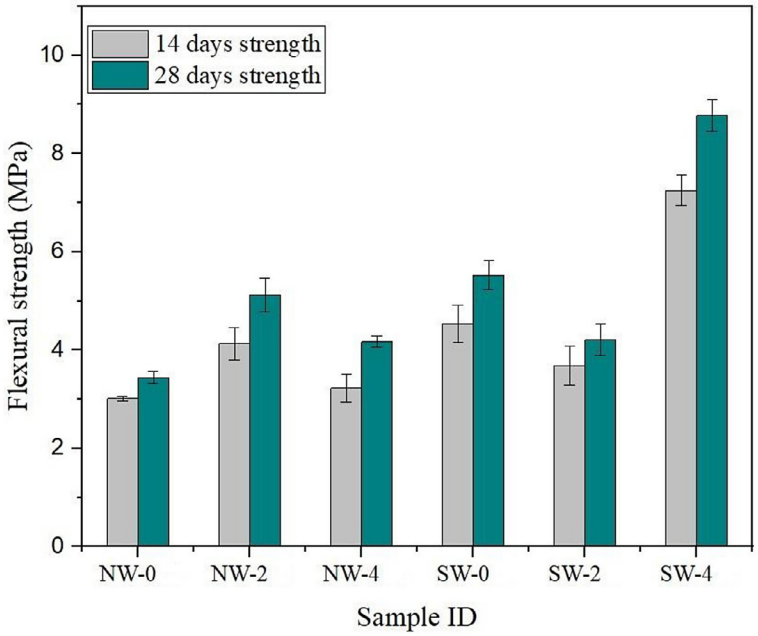

Figure 6. Flexural strength of normal water and seawater samples.

proper phase development in the early age strength. At 28 days, NW-2 exhibited the highest strength (5.12 MPa), outperforming both NW-0 (3.7 MPa) and NW-4 (4.2 MPa). This strength pattern confirms that the 2% addition of oxalic acid represents a threshold that balances iron dissolution and enhances the reaction kinetics through carbonation precipitation in the iron binders, leading to the strength development. The reduction in strength at 4% suggests that over-saturation effects lower the pH owing to increased acidity, suppressing iron carbonate crystallization, potentially interfering with binder and key carbonation mechanisms [51–53]. Unlike the NW samples, the SW samples exhibited an increase in strength with higher oxalic acid concentrations, linked to several synergistic effects. At 14 days, SW-0 attained 4.8 MPa, which decreased to 3.7 MPa (SW-2) and attained a peak value of 7.25 MPa (SW-4). This trend continued at 28 days of strength, as SW-4 demonstrated the highest flexural strength (8.77 MPa), followed by SW-2 (4.3 MPa) and SW-0 (5.52 MPa). The SW-4 samples showed a 20% increase in strength between 14 days and 28 days, suggesting that the carbonation reaction remained active over time. The superior performance of SW samples, particularly at 4% of oxalic acid, may be attributed to the chemical interactions between seawater minerals and oxalic acid. Oxalic acid behaves as a strong dissolution agent, promoting carbonation through iron dissolution [54]. The presence of chloride and sulphate ions in seawater likely promotes reaction kinetics by facilitating the precipitation of additional carbonation reaction products, which enhances the binder matrix properties [45]. Additionally, the continued availability of magnesium ions (Mg^{2+}) in seawater and Ca^{2+} ions contributes to the formation of magnesium-based products, such as hydromagnesite, and secondary mineralization, which improves the structural integrity and long-term performance, reinforcing its effectiveness as an iron binder [55, 56]. This shows that there is higher and sustained strength development observed in seawater-based iron binders compared to their normal water-based counterparts.

Correlation between compressive strength and flexural strength

The correlation between compression and flexural strength of samples at both 14 and 28 days is presented in Figure 7. As the compressive strength increases, the flexural strength also generally increases. A review of the data for both the 14-day and 28-day strengths reveals a consistent trend where higher compressive strength values are associated with higher flexural strength values [57, 58]. For instance, at 28 days, sample NW-0, which has the lowest compressive strength of 10.65 MPa, also exhibits the lowest flexural strength at 3.7 MPa. In contrast, sample SW-4 shows a high compressive strength of 17.93 MPa

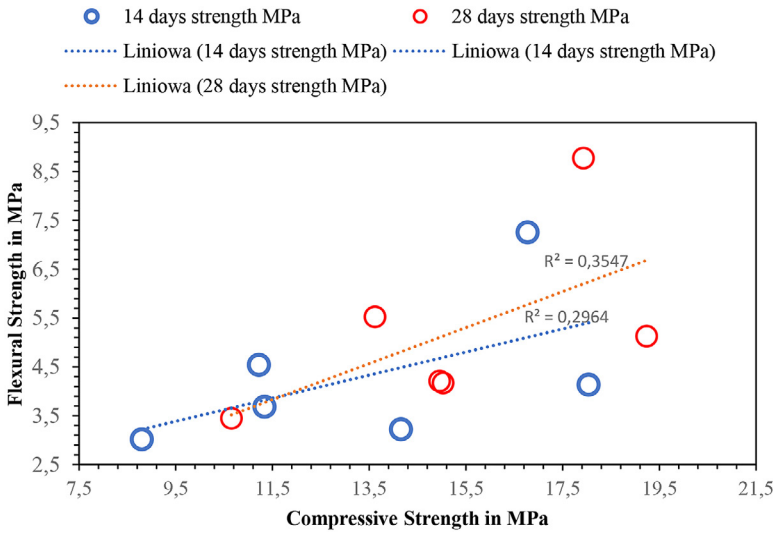

Figure 7. Relationship between compressive and flexural strengths.

and the highest flexural strength of 8.77 MPa. This direct relationship is expected, as the internal structure and properties of the material that lead to high resistance against crushing forces (compressive strength) also contribute to its ability to resist bending forces (flexural strength). While there is a clear positive trend, the ratios are not constant, indicating that the relationship is not perfectly linear. The flexural strength is consistently a fraction of the compressive strength, ranging from approximately 23% to 49% for the 28-day results.

When all six samples are considered, the correlation between flexural and compressive strength is relatively weak. This is quantified by the initial coefficient of determination (R^2) values of $R^2 = 0.2964$ and $R^2 = 0.3547$ on 14 and 28 days, respectively. These values indicate that only about 30-35% of the variability in flexural strength can be explained by the compressive strength. The scatter plot would show the data points dispersed loosely around a potential trendline, suggesting that other factors are influencing the results or that some data points do not follow the general trend. The samples NW-2 and NW-4 are identified as causing noise in the correlation. These two points act as outliers because they exhibit relatively high compressive strength but have proportionally lower flexural strength compared to the other samples in the dataset. At 28 days, sample NW-2 has the highest compressive strength (19.24 MPa), but its flexural strength (5.12 MPa) is lower than that of SW-0 (5.52 MPa) and significantly lower than SW-4 (8.77 MPa), both of which have lower compressive strengths. This deviation from the trend established by the other samples weakens the overall correlation.

Removing the outlier samples, NW-2 and NW-4, leads to a significant improvement in the correlation, demonstrating a much more consistent and predictable relationship for the remaining samples (NW-0, SW-0, SW-2, and SW-4). The R^2 values improve significantly from 0.2964 to 0.9545 on 14 days and from 0.3547 to 0.7536 on 28 days.

An R^2 of 0.9545 for the 14-day data indicates a very strong linear relationship. This means that for the remaining subset of samples, compressive strength can predict over 95% of the variation in flexural strength. Similarly, the improved R^2 of 0.7536 for the 28-day data shows a strong correlation. This substantial improvement suggests that the NW-2 and NW-4 samples may belong to a different population or were affected by experimental variables not present in the other samples. By isolating the more homogenous group of samples, a clearer and more reliable correlation between flexural and compressive strength is revealed.

Image processing

The impact of adding varying percentages of oxalic acid to normal water and seawater was significant, influencing the porosity and average pore radius of the samples, as shown in Figures 8 and 9. In normal water, the NW-2 sample exhibited the highest porosity (0.237), whereas NW-4 had the lowest porosity (0.1015). For the

seawater samples, SW-4 showed the highest porosity (0.3224), and SW-0 had the lowest porosity (0.1366). These variations in porosity directly affected structural characteristics and carbonation efficiencies of the samples. Well-distributed and fine structures were observed in samples NW-2 and NW-4, which increased the surface area for CO_2 diffusion, promoting more uniform carbonation and deeper penetration of CO_2 gas molecules during the curing process. While NW-4 showed the lowest porosity (0.1015), it also exhibited notable crystalline formation, as shown in Figure 10. This indicates that excessive Fe^{3+} ion chelation leads to a larger precipitation of reaction products filling the pores. The tortuous pores in the NW-2 and SW-4 samples slowed down the diffusion of CO_2, ensuring that more uniform carbonation proceeded gradually and homogeneously, minimizing unreacted zones throughout the iron binder matrix. In contrast, the NW-0 and SW-0 samples resulted in non-uniform carbonation due to the larger interconnected pores that allowed for faster CO_2 diffusion but left unreacted areas in the core section of the samples. Seawater samples generally exhibit more interconnected pores than normal water samples, with the presence of salts contributing to the precipitation of carbonation reaction products and the formation of stable carbonate phases. Notably, in SW-4, oxalic acid improved the structural integrity by mitigating interference from seawater. The presence of ions, including Mg^{2+}, Cl^- and SO_4^{2-}, in seawater was involved in the modification. The pore structure provides additional pathways for enhancing the reaction with oxalic acid [49]. The increase in porosity in the NW-0 and SW-0 samples led to reduced mechanical strength, highlighting the complex relationship between porosity, pore structure, and overall performance of the iron binder matrix.

Porosity during carbonation curing plays a crucial role in enhancing the reaction between CO_2 and the iron-based binder. By increasing the available surface area, this porosity accelerates the reaction kinetics, contributing to strength gain and the development of reaction products [59]. The SEM images revealed that the level of porosity of the binder matrices contained larger pores with irregular shapes, resulting in rough surface textures that disrupted the matrix continuity and led to the formation of larger voids [60]. However, these larger voids were excluded from porosity analysis because of their mode of formation. During carbonation curing, the precipitation of calcium and iron carbonates occurred within the pores, effectively reducing both the pore volume and porosity of the samples [61]. The precipitation of carbonates further blocks the

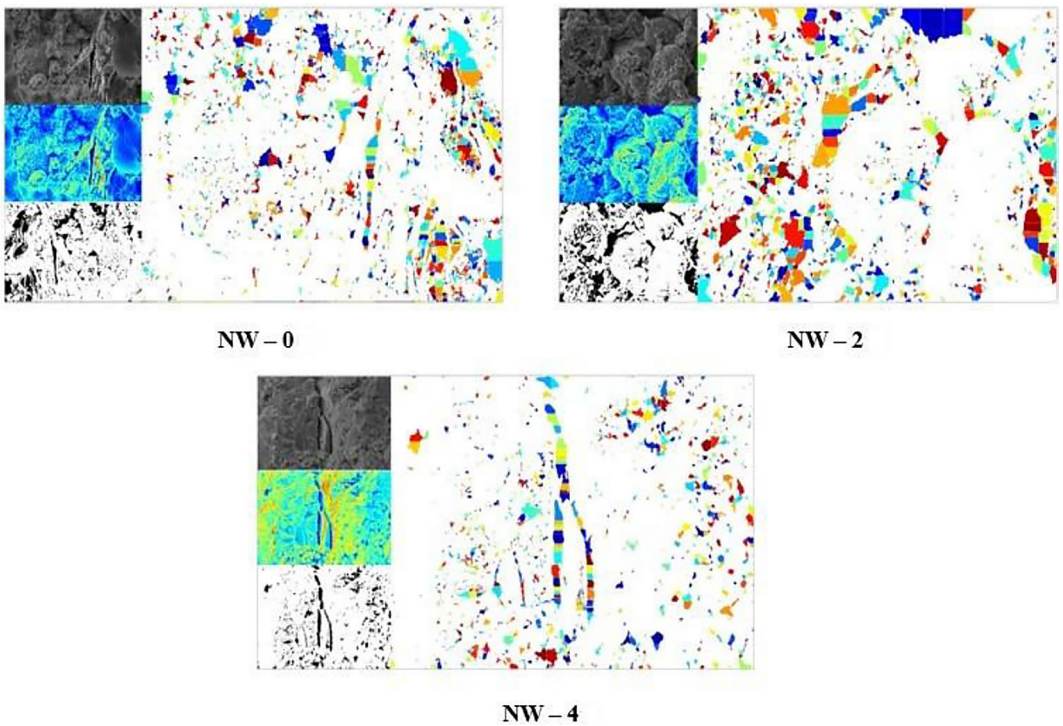

Figure 8. Image processing analysis for normal water samples

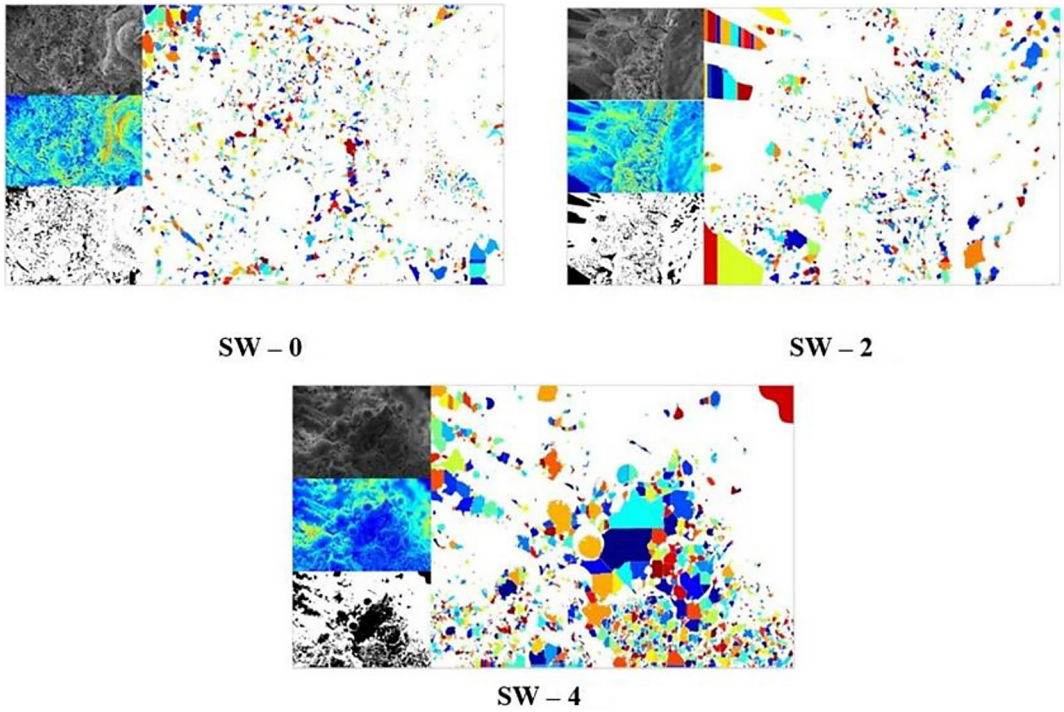

Figure 9. Image processing analysis for seawater samples

existing pores, leading to enhanced densification of the iron binders. As a result of these reactions, the overall structure becomes more compact and potentially attains higher mechanical properties. The reduced porosity and pore volume achieved through carbonate formation demonstrate the dynamic nature of the carbonation curing process and its impact on the microstructure of the iron-based binder [62, 63]. Consequently, the carbonation curing offers a promising approach for developing sustainable construction materials with enhanced performance characteristics. The non-correlation of pores to mechanical strength is due to the chelating effect of oxalic acid, which makes the fresh binder more reactive, and the pores are influenced by carbonate formation. The stable Fe (III) (Fe^{3+}) and other carbonates provide a binding effect, even though with a scattered microstructure. The agglomeration in a lesser oxalic acid concentration does not reflect in strength, as the products formed are not stable and offer binding properties. Hence, these observations show that the carbonation time and efficiency can be improved in future work.

Analysis of SEM images

The scanning electron microscope (SEM) images of the normal water sample are shown in Figure 11 (A to C), and the seawater sample is shown in Figure 12 (A to C). The observations reveal distinct differences in the microstructure of the iron-based binders, driven by the type of water and the concentration of oxalic acid under CO_2 curing conditions. NW-0 has the microstructure consisting of fine, globular, and poorly defined particles clustered together in porous agglomerates. This morphology is typical of rapidly precipitated, microcrystalline siderite ($FeCO_3$) [64]. The NW-2 sample shows a more integrated and dense structure compared to NW-0. The individual particles appear to have fused, forming larger, rounded masses, suggesting the oxalic acid has influenced the initial stages of crystal growth by enhancing Fe^{2+} ion formation and carbonate precipitation [20]. NW-4 exhibits a significant change, with the formation of dense, plate-like structures and a noticeable microcrack. The granular texture is replaced by a more consolidated, crystalline mass, indicating that a higher concentration of oxalic acid promotes the formation of larger, more ordered crystals, attributed to the excessive chelation effects of oxalic acid. SW-0, in contrast to its normal water counterpart (NW-0), displays a more complex morphology. Alongside granular particles, there are emerging rosette-like crystalline structures identified as hydromagesite, which is formed

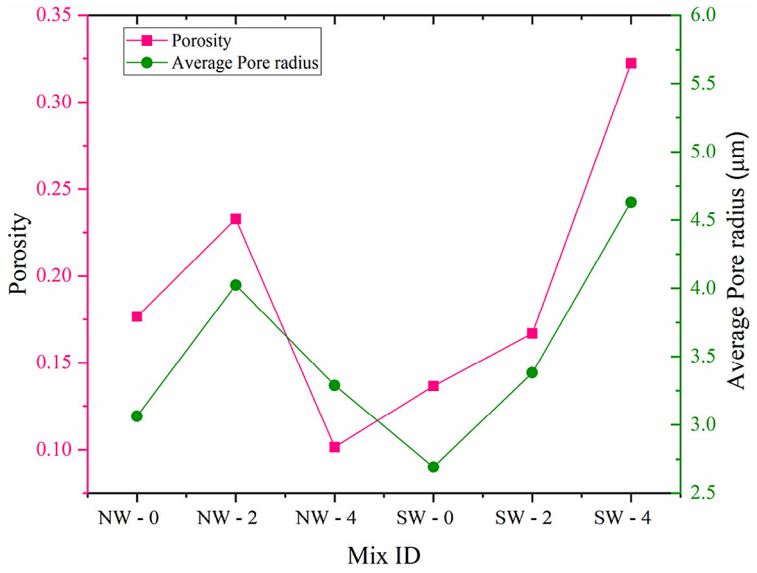

Figure 10. Porosity and Pore radius of normal water and seawater samples

through the reaction of Mg^{2+} ions present in seawater with CO_2 molecules, and begins to influence crystal formation even without oxalic acid [40]. The SW-2 sample exhibits a significantly different and highly organized microstructure. It is characterized by well-defined, needle-like crystals arranged in dense, interlocking clusters. This acicular (needle-like) morphology is a significant departure from the globular forms seen in the NW series. SW-4 has the morphology that shifts again, showing well-formed spherical particles of various sizes. Some spheres have a porous, honeycomb-like surface. This distinct spherical shape suggests a different crystalline phase or growth mechanism is dominant at this combination of seawater and high oxalic acid content, facilitating carbonate precipitation by modifying ion interactions [65].

The observed morphologies provide insights into the mineral phases in normal water and seawater samples. Siderite ($FeCO_3$) has the fine, granular, and globular structures seen in NW-0 and NW-2 are consistent with the typical appearance of microcrystalline siderite formed through ion interactions. Aragonite, which is distinct needle-like crystals in SW-2, is a polymorph of calcium carbonate, which is more likely to form in seawater. Ions like magnesium, which are abundant in seawater, inhibit the formation of the more common calcite and instead promote aragonite growth. Similarly, spherical particles in SW-4 are a classic morphology for vaterite, another polymorph of calcium carbonate[66, 67]. The formation of these distinct phases in the seawater samples is due to the presence of calcium, magnesium, and other dissolved ions that co-precipitate with the iron carbonate.

The SEM images clearly show that the samples made with seawater have more developed and organized crystalline structures compared to those made with normal water. This morphological improvement is due to the complex chemistry of seawater. While chloride is one component, the effect is largely driven by the presence of other ions like magnesium (Mg^{2+}) and sulfate (SO_4^{2-}). The ions in seawater, particularly Mg^{2+}, act as crystal habit modifiers. Magnesium ions are known to disrupt the formation of simple rhombohedral crystals, which are calcite, and instead promote the growth of more complex polymorphs like the needle-like aragonite observed in SW-2. Seawater provides a rich source of Ca^{2+} and Mg^{2+}, which can be incorporated into the carbonate structure during crystallization. This leads to the co-precipitation of more stable and well-ordered calcium carbonate phases (aragonite, vaterite) alongside the iron carbonate, resulting in a denser, more crystalline matrix [56, 68]. The dissolved ions in seawater can alter the kinetics of crystal nucleation and growth, serving as templates or catalysts, leading to the formation of the more intricate and organized structures observed in the SW samples compared to the relatively simple agglomerates in the NW samples.

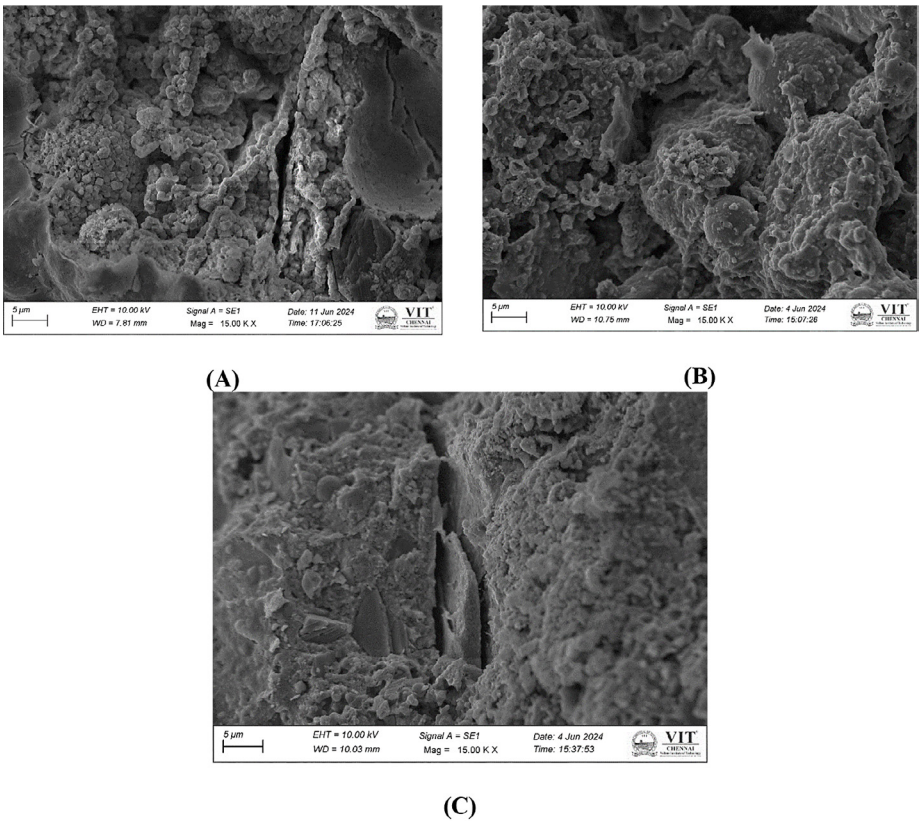

Figure 11. Scanning electron microscopy image of samples with normal water (A) 0 percent oxalic acid (NW-0), (B) 2 percent oxalic acid (NW-2), (C) 4 percent oxalic acid (NW-4)

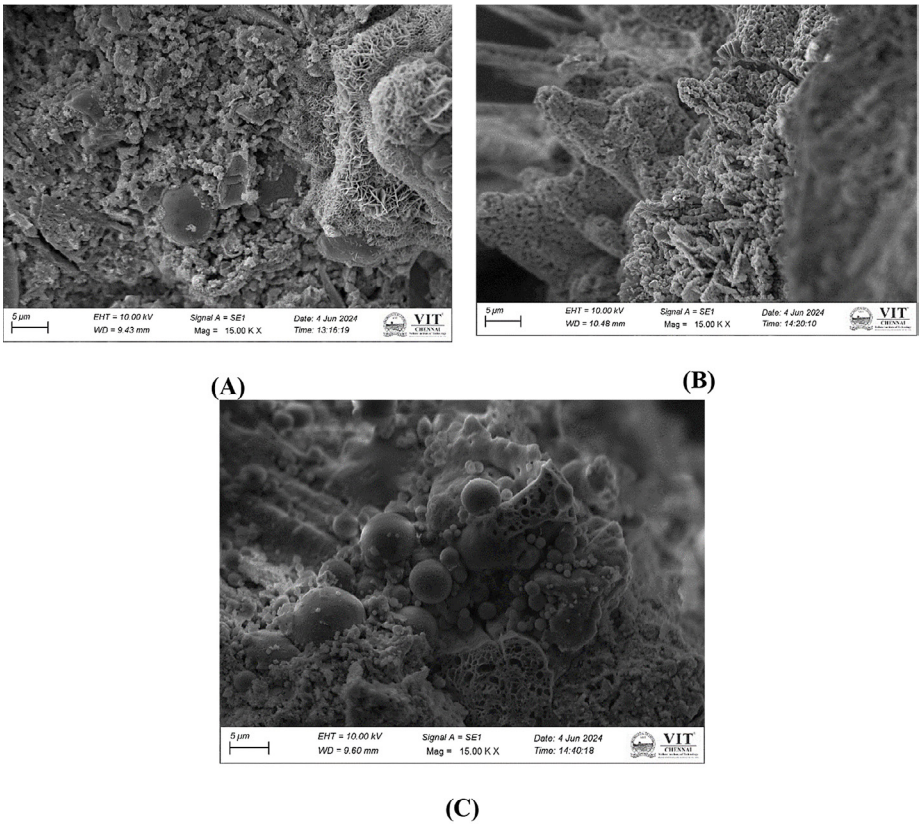

Figure 12. Scanning electron microscopy image of samples with seawater (A) 0 percent oxalic acid (SW-0), (B) 2 percent oxalic acid (SW-2), (C) 4 percent oxalic acid (SW-4)

CONCLUSIONS

This study demonstrates the potential of iron-based binders under CO_2 curing, yielding a sustainable construction material. The addition of oxalic acid to seawater as a mixing medium has yielded promising results for enhancing the mechanical properties and carbonation efficiencies. The key findings are as follows.

The highest strength gains are achieved at moderate oxalic acid concentrations, such as 2% in normal water samples and 4% in seawater samples, as it effectively facilitates iron dissolution, uniform CO_2 diffusion, effective carbonate formation, and the development of a dense matrix.

Excessive oxalic acid, as observed in 4% of normal water samples, can adversely affect the microstructure, resulting in increased porosity and weaker phases, thereby diminishing strength.

Seawater samples exhibited higher strength development at higher oxalic acid concentrations (4%) owing to the synergistic effect with ions in seawater, as well as additional reaction products such as hydromagnesite. The interaction with seawater ions, particularly magnesium and calcium, further amplifies carbonation and strength development, underscoring the importance of tailoring additive concentrations to specific water chemistries under CO_2 curing.

Excessive oxalic acid can lead to increased porosity due to precipitate filling and the formation of larger, irregular pores, which may compromise structural integrity. Seawater's mineral content further modifies pore connectivity and promotes stable carbonate formation, helping to improve the microstructure and strength of the binder.

Controlling porosity through the best oxalic acid addition and understanding seawater interactions is essential for developing sustainable and high-performance iron-based binders with superior structural characteristics.

Image processing analysis proved that the controlled formation of porosity plays a crucial role in uniform carbonation through diffusion of CO_2 molecules in well-distributed, delicate pore structures, promoting the effective carbonation reactions.

The use of seawater introduces a variety of ions that fundamentally change the crystallization pathway of the binder, leading to a more complex, organized, and robust microstructure. This is clearly demonstrated by the differences between the simple granular structures in the NW series and the well-defined crystalline morphologies in the SW series.

The precipitation of calcium and iron carbonates during carbonation curing led to a reduced pore volume, thereby enhancing densification and improving the mechanical properties.

In conclusion, tailoring oxalic acid concentration to the water chemistry is crucial for enhancing the mechanical and microstructural properties of iron-based binders, with seawater environments offering enhanced potential for strength development through chemical interactions and secondary mineral formation.

REFERENCES

1. Li S, Chen X, Hu M, et al. Carbon sequestration effects in cementitious composite binder materials under accelerated carbonation: A review. Materials Today Sustainability; 25. Epub ahead of print 1 March 2024. https://doi.org/10.1016/j.mtsust.2023.100663
2. Leonzio G, Shah N. Recent advancements and challenges in carbon capture, utilization and storage. Current Opinion in Green and Sustainable Chemistry; 46. Epub ahead of print 1 April 2024. https://doi.org/10.1016/j.cogsc.2024.100895
3. Ahmed O, Ahmad S, Adekunle SK. Carbon dioxide sequestration in cementitious materials: A review of techniques, material performance, and environmental impact. Journal of CO2 Utilization; 83. Epub ahead of print 1 May 2024. https://doi.org/10.1016/j.jcou.2024.102812
4. Neeraj, Yadav S. Carbon storage by mineral carbonation and industrial applications of CO2. Mater Sci Energy Technol 2020; 3: 494–500.
5. Liu W, Teng L, Rohani S, et al. CO_2 mineral carbonation using industrial solid wastes: A review of recent developments. Chemical Engineering Journal; 416. Epub ahead of print 15 July 2021. https://doi.org/10.1016/j.cej.2021.129093
6. Meng D, Unluer C, Yang EH, et al. Recent advances in magnesium-based materials: CO2 sequestration and utilization, mechanical properties and environmental impact. Cem Concr Compos; 138. Epub ahead of print 1 April 2023. https://doi.org/10.1016/j.cemconcomp.2023.104983
7. Jaffar MM, Rolfe A, Brandoni C, et al. A technical and environmental comparison of novel silica PEI adsorbent-based and conventional MEA-based CO_2 capture technologies in the selected cement plant. Carbon Capture Science and Technology; 10. Epub ahead of print 1 March 2024. https://doi.org/10.1016/j.ccst.2023.100179
8. Li N, Mo L, Unluer C. Emerging CO_2utilization technologies for construction materials: A review. Journal of CO2 Utilization; 65. Epub ahead of

print 1 November 2022. https://doi.org/10.1016/j.jcou.2022.102237

9. Shuto D, Igarashi K, Nagasawa H, et al. CO_2 fixation process with waste cement powder via regeneration of alkali and acid by electrodialysis: effect of operation conditions. Ind Eng Chem Res 2015; 54: 6569–6577.
10. Saranya V, Karthiyaini S, Stone D. Enhancement of strength and microstructural characterization in red mud-iron carbonate binders: Effects of CO_2 sequestration and oxalic acid concentration. Results in Engineering; 25. Epub ahead of print 1 March 2025. https://doi.org/10.1016/j.rineng.2025.104539
11. Zhang N, Deng G, Liao W, et al. Aqueous carbonation of steel slags: A comparative study on mechanisms. Cem Concr Compos; 155. Epub ahead of print 1 January 2025. https://doi.org/10.1016/j.cemconcomp.2024.105838
12. Wang YS, Ishak S, Zhang GZ, et al. Carbonation curing behavior and performance improvement of recycled coral waste concrete. Journal of Building Engineering; 90. Epub ahead of print 1 August 2024. https://doi.org/10.1016/j.jobe.2024.109473
13. Pan SY, Chen YH, Fan LS, et al. CO_2 mineralization and utilization by alkaline solid wastes for potential carbon reduction. Nat Sustain 2020; 3: 399–405.
14. Ma Z, Liao H, Wang L, et al. Effects of iron/silicon/magnesium/aluminum on CaO carbonation of CO_2 in steel slag-based building materials during carbonation curing. Constr Build Mater; 298. Epub ahead of print 6 September 2021. https://doi.org/10.1016/j.conbuildmat.2021.123889
15. Palanisamy S, Palanisami K, Madeshwaren V. Nano iron particles influence on mechanical properties and morphological analysis of polymer composites. Revista Materia; 30. Epub ahead of print 2025. https://doi.org/10.1590/1517-7076-RMAT-2024-0698
16. Mora Mendoza EY, Sarmiento Santos A, Vera López E, et al. Iron oxides as efficient sorbents for CO_2 capture. Journal of Materials Research and Technology 2019; 8: 2944–2956.
17. Nallusamy R, Rathinasamy S. Comparative analysis of nanoparticle-based nanofluids in heat pipes: enhancing thermal conductivity with graphene oxide, copper oxide, iron oxide, and titanium oxide. Revista Materia; 30. Epub ahead of print 2025. https://doi.org/10.1590/1517-7076-RMAT-2024-0577
18. Dhairiyasamy R, Bassi W, Jaganathan S, et al. The role of metal oxide nanoparticles in advancing sustainable energy systems with biodiesel blend. Revista Materia; 30. Epub ahead of print 2025. https://doi.org/10.1590/1517-7076-RMAT-2024-0979
19. Kumar S, Drozd V, Durygin A, et al. Capturing CO_2 Emissions in the iron industries using a magnetite-iron mixture. Energy Technology 2016; 4: 560–564.
20. Das S, Stone D, Convey D, et al. Pore- and microstructural characterization of a novel structural binder based on iron carbonation. Mater Charact 2014; 98: 168–179.
21. Li G, Yang J, Li H, et al. Enhancing sustainable utilization of iron-based alkaline solid wastes for carbon mineralization: Insights into CO_2 transport and adsorption dynamics. Developments in the Built Environment; 21. Epub ahead of print 1 March 2025. https://doi.org/10.1016/j.dibe.2024.100595
22. Kusin FM, Hasan SNMS, Molahid VLM, et al. Carbon dioxide sequestration of iron ore mining waste under low-reaction condition of a direct mineral carbonation process. Environmental Science and Pollution Research 2023; 30: 22188–22210.
23. Ji L, Yu H, Zhang R, et al. Effects of fly ash properties on carbonation efficiency in CO_2 mineralisation. Fuel Processing Technology 2019; 188: 79–88.
24. Xian X, Mahoutian M, Zhang D, et al. Carbon capture and utilization using cement-free concrete products via near-ambient pressure carbonation. International Journal of Greenhouse Gas Control; 134. Epub ahead of print 1 May 2024. https://doi.org/10.1016/j.ijggc.2024.104130
25. Li Y, Han D, Wang H, et al. Carbonation curing of mortars produced with reactivated cementitious materials for CO2 sequestration. J Clean Prod; 383. Epub ahead of print 10 January 2023. https://doi.org/10.1016/j.jclepro.2022.135501
26. Shao X, Qin B, Shi Q, et al. The impacts of CO_2 mineralization reaction on the physicochemical characteristics of fly ash: A study under different reaction conditions of the water-to-solid ratio and the pressure of CO_2. Energy; 287. Epub ahead of print 15 January 2024. https://doi.org/10.1016/j.energy.2023.129676
27. Das S, Kizilkanat AB, Chowdhury S, et al. Temperature-induced phase and microstructural transformations in a synthesized iron carbonate (siderite) complex. Mater Des 2016; 92: 189–199.
28. Sekar D, Udhayakumar KRB, Dyson C, et al. The influence of supplementary cementitious materials on concrete properties. Revista Materia; 30. Epub ahead of print 2025. https://doi.org/10.1590/1517-7076-RMAT-2024-0873
29. Ayyadurai A, Muthuchamy SM, Gopalakrishnan D, et al. A comprehensive comparative analysis of the impact of metakaolin and fly ash additions on the mechanical performance of fiber-reinforced concrete beams. Revista Materia; 30. Epub ahead of print 2025. https://doi.org/10.1590/1517-7076-RMAT-2024-0765
30. Jeon J, Kim MJ. CO_2 storage and $CaCO_3$ production using seawater and an alkali industrial by-product. Chemical Engineering Journal; 378. Epub ahead of print 15 December 2019. https://doi.org/10.1016/j.cej.2019.122180

31. Ding Z, Zhang X, Cheng T, et al. Unlocking high carbonation efficiency: Direct CO_2 mineralization with fly ash and seawater. Chem Eng Sci; 282. Epub ahead of print 5 December 2023. https://doi.org/10.1016/j.ces.2023.119349
32. Li H, Zhang R, Wang T, et al. Performance evaluation and environment risk assessment of steel slag enhancement for seawater to capture CO_2. Energy; 238. Epub ahead of print 1 January 2022. https://doi.org/10.1016/j.energy.2021.121861
33. Li Y, Liu W, Mi T, et al. Durability study of seawater and sea-sand concrete under the combined effects of carbonation and chloride redistribution. Journal of Building Engineering; 89. Epub ahead of print 15 July 2024. https://doi.org/10.1016/j.jobe.2024.109294
34. Lee SO, Tran T, Park YY, et al. Study on the kinetics of iron oxide leaching by oxalic acid. Int J Miner Process 2006; 80: 144–152.
35. Lee SO, Tran T, Jung BH, et al. Dissolution of iron oxide using oxalic acid. Hydrometallurgy 2007; 87: 91–99.
36. Prentice LH, Tyas M. The effect of oxalic acid incorporation on the setting time and strength of a glass-ionomer cement. Acta Biomater 2006; 2: 109–112.
37. Rabbani A, Salehi S. Dynamic modeling of the formation damage and mud cake deposition using filtration theories coupled with SEM image processing. J Nat Gas Sci Eng 2017; 42: 157–168.
38. Vellapandi V, Muthusamy S. Influence of metasteatite on strength and porosity of magnesium oxychloride cement: An experimental and image processing approach. Revista Materia; 29. Epub ahead of print 2024. https://doi.org/10.1590/1517-7076-RMAT-2024-0634
39. Loder A, Siebenhofer M, Böhm A, et al. Clean iron production through direct reduction of mineral iron carbonate with low-grade hydrogen sources; the effect of reduction feed gas composition on product and exit gas composition. Clean Eng Technol; 5. Epub ahead of print 1 December 2021. https://doi.org/10.1016/j.clet.2021.100345
40. Chandralega V, Shanmugasundaram M, Stone D. Enhancing the performance of iron-based binders with seawater and CO_2 sequestration. Case Studies in Construction Materials; 22. Epub ahead of print 1 July 2025. https://doi.org/10.1016/j.cscm.2025.e04367
41. Das S, Souliman B, Stone D, et al. Synthesis and properties of a novel structural binder utilizing the chemistry of iron carbonation. ACS Appl Mater Interfaces 2014; 6: 8295–8304.
42. Das S, Stone D, Mobasher B, et al. Strain energy and process zone based fracture characterization of a novel iron carbonate binding material. Eng Fract Mech 2016; 156: 1–15.
43. Al-Anezi K, Hilal N. Effect of carbon dioxide in seawater on desalination: A comprehensive review. Separation and Purification Reviews 2006; 35: 223–247.
44. Kim D, Kim M. Study on carbon dioxide storage through mineral carbonation using sea water and paper sludge ash. Journal of the Korean Society for Marine Environment and Energy 2016; 19: 18–24.
45. Li H, Tang Z, Xing X, et al. Study of CO_2 capture by seawater and its reinforcement. Energy 2018; 164: 1135–1144.
46. Saxena S, Baghban MH. Seawater concrete: A critical review and future prospects. Developments in the Built Environment; 16. Epub ahead of print 1 December 2023. https://doi.org/10.1016/j.dibe.2023.100257
47. Kuang L, Li G, Xiang J, et al. Effect of seawater on the properties and microstructure of metakaolin/slag-based geopolymers. Constr Build Mater; 397. Epub ahead of print 15 September 2023. https://doi.org/10.1016/j.conbuildmat.2023.132418
48. Ho HJ, Iizuka A. Mineral carbonation using seawater for CO_2 sequestration and utilization: A review. Separation and Purification Technology; 307. Epub ahead of print 15 February 2023. https://doi.org/10.1016/j.seppur.2022.122855
49. Saleh S, Mahmood AH, Hamed E, et al. The mechanical, transport and chloride binding characteristics of ultra-high-performance concrete utilising seawater, sea sand and SCMs. Constr Build Mater; 372. Epub ahead of print 3 April 2023. https://doi.org/10.1016/j.conbuildmat.2023.130815
50. Ho HJ, Iizuka A. Mineral carbonation using seawater for CO_2 sequestration and utilization: A review. Separation and Purification Technology; 307. Epub ahead of print 15 February 2023. https://doi.org/10.1016/j.seppur.2022.122855
51. Kahyarian A, Brown B, Nesic S. Electrochemistry of CO_2 corrosion of mild steel: Effect of CO_2 on iron dissolution reaction. Corros Sci 2017; 129: 146–151.
52. Das S, Hendrix A, Stone D, et al. Flexural fracture response of a novel iron carbonate matrix - Glass fiber composite and its comparison to Portland cement-based composites. Constr Build Mater 2015; 93: 360–370.
53. Nayak S, Krishnan NMA, Das S. Fracture response of metallic particulate-reinforced cementitious composites: Insights from experiments and multiscale numerical simulations. Cem Concr Compos 2019; 97: 154–165.
54. [Santawaja P, Kudo S, Tahara A, et al. Dissolution of iron oxides highly loaded in oxalic acid aqueous solution for a potential application in iron-making. ISIJ International 2022; 62: 2466–2475.

55. Liu X, Chen Z, Yu Z, et al. A review on ultra-high performance seawater sea sand concrete: Hydration, microstructure and properties. Construction and Building Materials; 438. Epub ahead of print 9 August 2024. https://doi.org/10.1016/j.conbuildmat.2024.136945
56. Kim S, Koh E, Kim MJ. Recovery of high-purity hydromagnesite from seawater through carbonation using $Ca(OH)_2$. Desalination; 586. Epub ahead of print 1 October 2024. https://doi.org/10.1016/j.desal.2024.117907
57. Kaya M, Koksal F, Gencel O, et al. Influence of micro Fe_2O_3 and MgO on the physical and mechanical properties of the zeolite and kaolin based geopolymer mortar. Journal of Building Engineering; 52. Epub ahead of print 15 July 2022. https://doi.org/10.1016/j.jobe.2022.104443
58. Kaya M, Köksal F. Physical and mechanical properties of C class fly ash based light-weight geopolymer mortar produced with expanded vermiculite aggregate. Revista de la Construccion 2022; 21: 21–35.
59. Polettini A, Pomi R, Stramazzo A. Carbon sequestration through accelerated carbonation of BOF slag: Influence of particle size characteristics. Chemical Engineering Journal 2016; 298: 26–35.
60. Miao E, Du Y, Zheng X, et al. Kinetic analysis on CO_2 sequestration from flue gas through direct aqueous mineral carbonation of circulating fluidized bed combustion fly ash. Fuel; 342. Epub ahead of print 15 June 2023. https://doi.org/10.1016/j.fuel.2023.127851
61. Gu H, Yang Z, Tao Y, et al. The influence of SCMs on the pore structure evolution and carbonation of cement pastes under early carbonization. Constr Build Mater; 465. Epub ahead of print 28 February 2025. https://doi.org/10.1016/j.conbuildmat.2025.140194
62. Choisez L, Hemke K, Özgün Ö, et al. Hydrogen-based direct reduction of combusted iron powder: Deep pre-oxidation, reduction kinetics and microstructural analysis. Acta Mater; 268. Epub ahead of print 15 April 2024. https://doi.org/10.1016/j.actamat.2024.119752
63. Li L, Chen T, Gao X. Synergistic effect of CO_2-mineralized steel slag and carbonation curing on cement paste. Cem Concr Compos; 145. Epub ahead of print 1 January 2024. https://doi.org/10.1016/j.cemconcomp.2023.105357
64. Srivastava S, Snellings R, Meynen V, et al. Siderite-calcite ($FeCO_3$–$CaCO_3$) series cement formation by accelerated carbonation of CO_2(g)–H_2O–Fe–$Ca(OH)_2$ systems. Cem Concr Compos; 122. Epub ahead of print 1 September 2021. https://doi.org/10.1016/j.cemconcomp.2021.104137
65. Rausis K, Ćwik A, Casanova I. Phase evolution during accelerated CO_2 mineralization of brucite under concentrated CO_2 and simulated flue gas conditions. Journal of CO_2 Utilization 2020; 37: 122–133.
66. Kang D, Lee MG, Jo H, et al. Carbon capture and utilization using industrial wastewater under ambient conditions. Chemical Engineering Journal 2017; 308: 1073–1080.
67. Azdarpour A, Afkhami Karaei M, Hamidi H, et al. CO_2 sequestration through direct aqueous mineral carbonation of red gypsum. Petroleum 2018; 4: 398–407.
68. Pokrovsky OS. Kinetics of $CaCO_3$ homogeneous precipitation in seawater.